J. Fluid Mech. (1998), *vol.* 362, *pp.* 177–198. Printed in the United Kingdom

Lagrangian frequency spectra of vertical velocity and vorticity in high-Reynolds-number oceanic turbulence

By REN-CHIEH LIEN, ERIC A. D'ASARO
AND GEOFFREY T. DAIRIKI

Applied Physics Laboratory, University of Washington, Seattle, WA 98105, USA

(Received 3 April 1997 and in revised form 23 December 1997)

Lagrangian properties of oceanic turbulent boundary layers were measured using neutrally buoyant floats. Vertical acceleration was computed from pressure (depth) measured on the floats. An average vertical vorticity was computed from the spin rate of the float. Forms for the Lagrangian frequency spectra of acceleration, $\Phi_a(\omega)$, and the Lagrangian frequency spectrum of average vorticity are found using dimension analysis. The flow is characterized by a kinetic energy dissipation rate, ε, and a large-eddy frequency, ω_0. The float is characterized by its size. The proposed non-dimensionalization accurately collapses the observed spectra into a common form. The spectra differ from those expected for perfect Lagrangian measurements over a substantial part of the measured frequency range owing to the finite size of the float. Exact theoretical forms for the Lagrangian frequency spectra are derived from the corresponding Eulerian wavenumber spectra and a wavenumber–frequency distribution function used in previous numerical simulations of turbulence. The effect of finite float size is modelled as a spatial average. The observed non-dimensional acceleration and vorticity spectra agree with these theoretical predictions, except for the high-frequency part of the vorticity spectrum, where the details of the float behaviour are important, but inaccurately modelled. A correction to the exact Lagrangian acceleration spectra due to measurement by a finite-sized float is thus obtained. With this correction, a frequency range extending from approximately one decade below ω_0 to approximately one decade into the inertial subrange can be resolved by the data. Overall, the data are consistent with the proposed transformation from the Eulerian wavenumber spectrum to the Lagrangian frequency spectrum. Two parameters, ε and ω_0, are sufficient to describe Lagrangian spectra from several different oceanic turbulent flows. The Lagrangian Kolmogorov constant for acceleration, $\beta_a \equiv \Phi_a/\varepsilon$, has a value between 1 and 2 in a convectively driven boundary layer. The analysis suggests a Lagrangian frequency spectrum for vorticity that is white at all frequencies in the inertial subrange and below, and a Lagrangian frequency spectrum for energy that is white below the large-eddy scale and has a slope of −2 in the inertial subrange.

1. Introduction

The Lagrangian properties of turbulence, although important in understanding turbulent dispersion, are rarely measured. Measurements of Lagrangian spectra, that is frequency spectra of quantities following a water parcel, are particularly rare.

Dimensional analysis can give a first guess as to the expected forms for Lagrangian spectra. We first review the well-known analysis for the Eulerian wavenumber spectrum of turbulent velocity in the inertial subrange. For scales much smaller than the forcing scales and much larger than the dissipation scales, Kolmogorov (1941) predicted the existence of an inertial subrange, characterized by a turbulent kinetic energy dissipation rate ε. The kinetic energy wavenumber spectrum has a form of $\alpha\varepsilon^{2/3}k^{-5/3}$, where k is the wavenumber magnitude and α is a Kolmogorov constant. In a recent review, Sreenivasan (1995) shows that modern data clearly support the existence of the '-5/3' spectrum and finds $\alpha = 1.5 \pm 0.15$ at high Reynolds number. The turbulence energy spectrum at very high Reynolds number is often approximated as

$$E(k) = \begin{cases} \alpha\varepsilon^{2/3}k^{-5/3}, & k_0 \leqslant k \leqslant k_\eta \\ 0, & k < k_0 \text{ or } k > k_\eta, \end{cases} \tag{1.1}$$

where k is the wavenumber magnitude and details near the large-eddy scale, k_0^{-1}, and the viscous dissipation (Kolmogorov) scale, k_η^{-1} have been neglected.

Similar arguments have been used to predict Lagrangian frequency spectra. Throughout this paper, the term 'frequency' will always mean 'Lagrangian frequency'. In an inertial subrange where the frequency spectrum depends only on frequency, ω, and ε, Corrsin (1963) predicted a white vertical acceleration spectrum with a level proportional to ε, i.e. $\Phi_a(\omega) = \beta_a\varepsilon$. Tennekes & Lumley (1972) predicted $\beta_a = 1.2$ by conserving energy in both the frequency and wavenumber domains and assuming the relation $\omega = \varepsilon^{1/3}k^{2/3}$ between frequency and wavenumber. They also suggested an ω^2 (blue) acceleration spectrum for frequencies below the inertial subrange, i.e.

$$\Phi_a^{TL}(\omega) = \begin{cases} \beta_a\varepsilon(\omega/\omega_0)^2 & \text{for } \omega \leqslant \alpha^{1/2}\omega_0 \\ \beta_a\varepsilon & \text{for } \omega > \alpha^{1/2}\omega_0, \end{cases} \tag{1.2}$$

where $\omega_0 = \varepsilon^{1/3}k_0^{2/3}$ is the frequency corresponding to the cutoff wavenumber of the inertial subrange. Our definition of ω_0 differs from theirs by a factor $\alpha^{1/2}$, where α is the Kolmogorov constant defined above.

Previous studies have found a white acceleration frequency spectrum but with a wide range of β_a, 0.2–1.2. Using a Lagrangian renormalized approximation, Kaneda (1993) derived a Lagrangian frequency spectrum in the inertial subrange with $\beta_a = 0.94$. In their kinematic simulations of turbulence, Fung *et al.* (1992) found $\beta_a = 0.8$ 'following a fluid particle', and $\beta_a = 0.73$ 'moving with the large eddies'. Hanna (1981) compared Lagrangian and Eulerian velocity measurements in a daytime atmospheric boundary layer and found $\beta_a = 0.2$, with large errors. Some of the variation in these estimates of β_a may be due to differences in definition. Fung *et al.* (1992) (their equation (2.28)) and Kaneda (1993) (his equation (22)) appear to use two-sided spectra, i.e. the velocity variance is $\int_{-\infty}^{\infty}\Phi_w(\omega)\mathrm{d}\omega$, whereas Tennekes & Lumley (1972) and Hanna (1981) use one-sided spectra, i.e. the velocity variance is $\int_0^{\infty}\Phi_w(\omega)\,\mathrm{d}\omega$. We prefer one-sided spectra, implying that the two Fung *et al.* (1992) estimates and the Kaneda (1993) estimate should be doubled to 1.6, 1.46 and 1.8 respectively. The Hanna (1981) paper and the associated data report (Hanna 1980) differ as to whether radial or cyclic units are being used in the spectral computations. Our best guess is that Hanna's (1981) value should be multiplied by 2π to equal 1.26. These corrections, which seem plausible but not certain, narrow the range for β_a to between 1 and 2, consistent with the range found in § 7 of this paper.

Lagrangian frequency spectra of vorticity, ζ, are rarely discussed in previous studies. Naively assuming an inertial subrange in which the vorticity spectrum depends only on ω and ε yields a vorticity spectrum, $\beta_\zeta\omega$ that is blue and independent of ε. In this paper, we show that vorticity spectra are white in the inertial subrange. This is dimensionally possible because another parameter, either the probe size or the Kolmogorov scale, necessarily enters the analysis.

Lagrangian frequency spectra of turbulence, unlike Eulerian spectra, have rarely been observed owing to instrumental difficulties. D'Asaro *et al.* (1996, hereafter referred to as DFOD) described a neutrally buoyant mixed layer float (MLF) designed for Lagrangian measurements of oceanic turbulence. In a brief look at spectra, DFOD found that both acceleration and vorticity spectra exhibited universal forms which scaled with ε, implying inertial-subrange scaling. In this paper, we examine these spectra in more detail.

We will analyse the data within the framework of homogeneous, statistically stationary turbulence theory. The Lagrangian frequency spectra and Eulerian wavenumber spectra are projections of a joint Lagrangian frequency–Eulerian wavenumber spectrum, $\Phi_u(\omega,\boldsymbol{k})$. Consider a Lagrangian trajectory, $\boldsymbol{x}_0(t)$, and the coordinate system $\boldsymbol{x}_L = \boldsymbol{x}-\boldsymbol{x}_0(t)$ that moves with it; $\Phi_u(\omega,\boldsymbol{k})$ is defined in this moving coordinate system. The velocity covariance $C_u(\boldsymbol{r},\tau)$ for a single velocity component u in this coordinate system is

$$C_u(\boldsymbol{r},\tau) = \langle u[t,\boldsymbol{x}_L(t)]\, u[t+\tau,\boldsymbol{x}_L(t+\tau)+\boldsymbol{r}]\rangle, \tag{1.3}$$

where $\langle\ \rangle$ represents ensemble averaging and τ and $\boldsymbol{r}$ are time and spatial lags. The Lagrangian frequency–Eulerian wavenumber velocity spectrum is defined as the Fourier transform of $C_u(\boldsymbol{r},\tau)$, i.e.

$$\Phi_u(\omega,\boldsymbol{k}) = \int_0^\infty \mathrm{d}\boldsymbol{r} \int_0^\infty \mathrm{d}\tau\, C_u(\boldsymbol{r},\tau)\mathrm{e}^{\mathrm{i}(\boldsymbol{k}\cdot\boldsymbol{r}-\omega\tau)}, \tag{1.4}$$

where $\boldsymbol{k}$ is the wavenumber vector and ω is the Lagrangian frequency. The integral of $\Phi_u(\omega,\boldsymbol{k})$ over wavenumber–frequency space equals the average variance of u in physical space.

In the next two sections, we briefly describe the MLF configuration, sensors, and measurements and show observed Lagrangian frequency spectra of vertical acceleration and vorticity. These spectra appear to have universal shapes. In § 4, we revisit the dimensional analysis adding the effect of finite float size. The Lagrangian spectral forms are derived from (1.1) in § 5 where we construct a joint Lagrangian frequency–Eulerian wavenumber spectrum for turbulence and model the averaging effect of finite-sized floats. In § 6, we fit the derived acceleration spectrum to the observed acceleration spectra, thus estimating ε and ω_0 for each spectrum. We then scale the observed acceleration and vorticity spectra by these parameters and show, first, that the observed spectra have common shapes and, second, that these shapes mostly agree with the model predictions. This allows us to identify the frequency range in which instrumental effects are important and compensate for these effects in the analysis. In § 7, β_a is estimated from the spectral level and the buoyancy flux in a convectively driven mixed layer. In the final two sections, we discuss the accuracy of the models and summarize the results.

2. Instrumentation and measurements

Measurements of Lagrangian trajectories were made using Lagrangian floats (MLF). Physically, the MLF consists of a 1.5 m long cylindrical hull and a 1.2 m diameter perforated (42% hole area) drag screen (figure 1). The float measures its

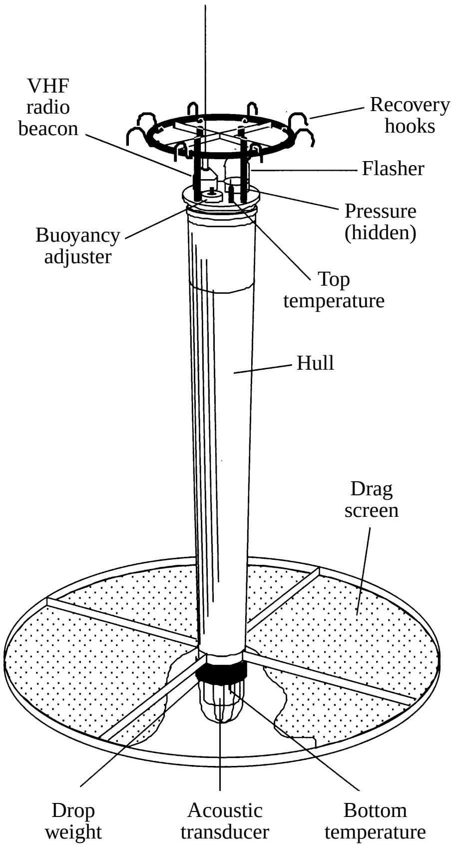

FIGURE 1. The mixed layer Lagrangian float.

own depth through pressure (1 Hz rate) and is acoustically tracked in the horizontal. Temperature and stratification are measured every 5 s using thermistors on the top and bottom of the float. The float has a large restoring moment which keeps it vertical to within few degrees. The rotational motion of the float is coupled to that of the water by the drag screen with a time constant of a few seconds. The coupling is due to both the roughness of the screen and its radial ribs which act as vertical fins. The spin rate of the float, measured by a compass every 5 s, gives an average vertical vorticity of the water.

The MLF is not perfectly Lagrangian, for several reasons. First, it is much larger than the Kolmogorov scale and can therefore, at best, follow the motion of a well-defined volume of water surrounding it, rather than the motion of an individual molecule. Second, the float's density differs from that of the surrounding water and it will therefore rise or fall relative to the water. We minimize the density difference at fixed pressure and temperature by careful ballasting. Subsequent density changes resulting from changes in the ambient pressure and temperature are minimized by approximately matching the float's compressibility and thermal expansion coefficients to that of sea water. The large drag screen reduces the fall rate due to any residual density difference to a few mm s^{-1} (see DFOD). Third, the float is asymmetrical. The hydrodynamic force on the float is not directly opposed to the relative velocity of the water, so the float can move in unexpected directions in the presence of strong

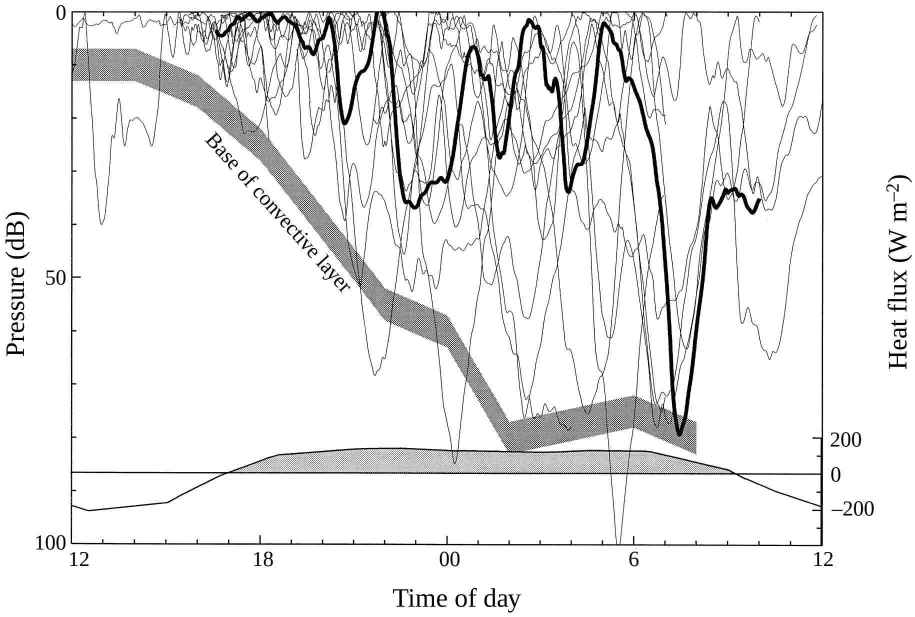

FIGURE 2. Depth of floats deployed in a diurnally varying convective mixed layer over a 1 week period. One trajectory is shown with a darker line. The average surface heat flux estimated from meteorological instruments is plotted at the bottom. The average depth of the convective layer, estimated from the depth of a very weak maximum in stratification measured from a vertical profiler is shown by the shaded region.

shear. We have observed this behaviour using scale model floats in a laboratory tank. Finally, since the float's sensors are offset from its centre, they do not follow a Lagrangian trajectory when the centre of the float does.

The Lagrangian accuracy of the floats has been tested by deploying them in flows where the exact Lagrangian trajectories are well known. In linear surface waves, pressure is constant along Lagrangian trajectories. DFOD describe measurements made on a float deployed in a known surface wave field. Pressure fluctuations were due only to the offset of the pressure sensor from the float's centre with no evidence of pressure fluctuations due to non-Lagrangian motion. The floats therefore accurately filter out surface wave vertical velocities and can accurately measure vertical velocity in the presence of surface waves. The surface wave and turbulent velocity signals can be further separated since their dominant frequencies typically differ by more than an order of magnitude. This is important in the upper ocean, where the surface gravity wave velocity, $O(1 \text{ m s}^{-1})$, is much greater than the turbulent velocity, $O(0.01 \text{ m s}^{-1})$.

Internal waves can exist only for frequencies less than the buoyancy frequency N. Temperature, θ, is nearly constant along the Lagrangian trajectories since the waves are nearly adiabatic. DFOD describe data from a float deployed in the upper oceanic thermocline. The vertical velocity spectrum falls by 4 orders of magnitude in the octave higher than N, indicating that the vertical velocity is mostly due to internal waves. The temperature fluctuations, θ', were converted to cross-isothermal velocity fluctuations using $w_c = (\mathrm{d}\theta'/\mathrm{d}t)/(\partial\theta/\partial z)$. The r.m.s. w_c was 0.1 mm s^{-1}, less than 2% of the r.m.s. vertical velocity. The floats are therefore highly Lagrangian in this environment.

In a turbulent flow of finite vertical extent, Lagrangian trajectories should fill the turbulent region but avoid the surrounding laminar fluid. The surface mixed layer of the ocean is such a flow. The trajectories of floats deployed in the mixed layer clearly delineate the turbulent region in both convectively driven mixed layers (figure 2) and wind-driven mixed layers (D'Asaro & Dairiki 1997).

In this paper we analyse data from 71 float deployments in a variety of highly turbulent oceanic environments; 21 trajectories are from a convectively driven upper-ocean mixed layer (figure 2), 36 are from a wind-driven mixed layer of similar depth, and 14 are from highly turbulent weakly stratified tidal channels similar to those used in the study by Grant, Stewart & Moilliet (1962). These data were selected from about 250 float deployments. Sections of trajectories were chosen to be from weakly stratified environments, to exhibit nearly stationary statistics and to have vertical excursions of at least 50 m. Most of the data excluded were taken in environments with strong stratification or weak forcing, or involved floats which were poorly ballasted. Data with anomalous spectral shapes were not intentionally excluded.

3. Observed spectra of vertical acceleration and vorticity

The pressure on the float measures its depth since pressure in the ocean is highly hydrostatic. Vertical displacement, Z, is thus easily computed from pressure (see §2 for a discussion of the effects of surface waves, which are not hydrostatic). Vertical velocity was computed from the time derivative of displacement and the vertical acceleration from the second derivative. The derivative at time i was estimated from the first difference $Z_i - Z_{i+1}$. All spectra were corrected for the response function of this operator. Vertical vorticity was estimated from compass direction using a similar first difference modified to account for the 2π-periodicity of direction.

Previous turbulence studies (Melville 1996) have shown strong intensification of turbulence within a few metres of the ocean surface when the wind is blowing. The float data show a similar increases in vorticity and acceleration variance very near the surface. These produce large and rapid variations in these properties as the float moves into and out of the surface layer. In this paper, we wish to study the more homogeneous turbulence in the rest of the boundary layer and therefore need to exclude the near-surface region. This is achieved using a maximum-overlap wavelet method (Percival & Guttorp 1994). The acceleration and vorticity time series are decomposed into a set of orthogonal wavelets, w_{ij}, each of which is compact in both time and frequency. Thus acceleration is represented as $a(t) = \sum_{i,j} a_{ij} w_{ij}(t)$. The variance centred at frequency j and time i is a_{ij}^2. The spectral density is the variance divided by the appropriate frequency bandwidth; its time average is the frequency spectrum. For the wind-driven and convective mixed layers, wavelet coefficients with an average depth shallower than 15 m were excluded from the average, resulting in a frequency spectrum that excludes near-surface data. The process is imperfect, since the low-frequency wavelet estimates necessarily have little time resolution and therefore include both near-surface and deep data. We hope this effect is small, since the near-surface enhancement of turbulence appears primarily at high frequencies. The resulting frequency spectra are shown in figures 3 and 4.

Vertical acceleration spectra have a large (3×10^4) range in spectral level (figure 3) corresponding, as will be shown, to a similarly large range in ε. The data fall into two groups. The more energetic are from turbulent tidal channels (solid lines), and the less energetic are from wind-forced (dotted lines) and convectively forced (dashed lines) oceanic mixed layers. Despite the large range in energy level and type of forcing, the

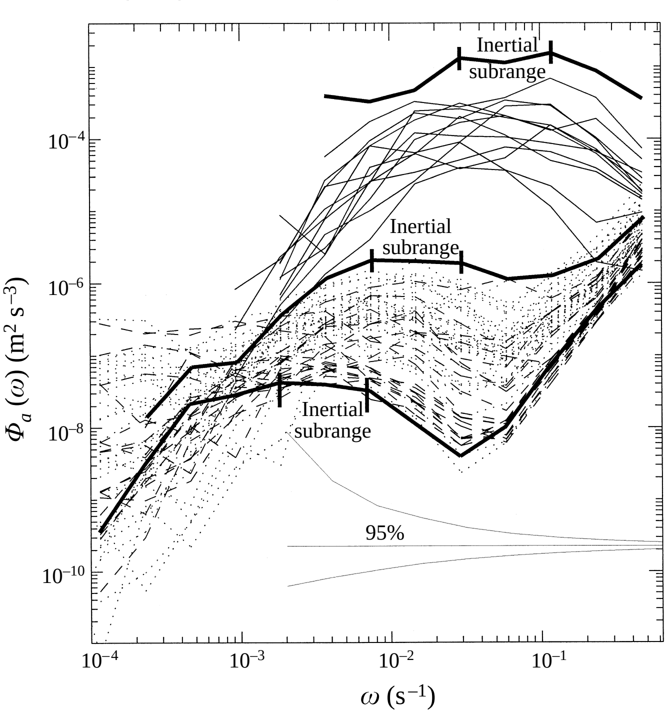

FIGURE 3. Lagrangian frequency spectra of vertical acceleration. Data from weakly stratified tidal channels is shown by solid lines. Data from upper-ocean mixed layers is separated by cruise: data from *Tully '92* is dashed, while data from *Wecoma '95* is dotted. The spectral estimate at the lowest frequency in each spectrum has 2 degrees of freedom; this doubles at each successive frequency. The 95% confidence limits with this dependence, starting at 2 degrees of freedom are shown at the bottom of the figure. For clarity, several spectra are highlighted (thick solid lines), and the approximate frequency band of the inertial subrange is labelled.

spectra have very similar shapes. We will show that the flat region at intermediate frequencies in the acceleration spectrum is a piece of the Lagrangian inertial subrange. The high-frequency limit of the range is set by the size of the float; the spectrum of float motion falls below the inertial subrange level at high frequencies because the float cannot follow water motions smaller than its own size. The low-frequency limit is set by the large-eddy frequency, ω_0. At frequencies well below ω_0, the spectra have a slope of approximately $+2$; vertical velocity is white as predicted by (1.2). At the highest frequencies many acceleration spectra have a slope of $+4$, corresponding to a white displacement spectrum. This is due to pressure sensor noise.

Vertical vorticity spectra show a smaller range of levels (figure 4) since, as will be shown, they scale with $\varepsilon^{1/3}$. All spectra have a similar shape. We will show that they are white both in the inertial subrange and at low frequencies with no signature of the large-eddy frequency, ω_0. Thus the low-frequency limit of the inertial subrange is not obvious from the spectrum. As with acceleration, the high-frequency limit of the inertial subrange is set by the size of the float; the spectrum of float rotation falls below the inertial subrange level for vertical vorticity because the float's rotation cannot follow vorticity fluctuations smaller than the size of the drag screen. The noise level for vorticity, evident at frequencies greater than about 0.1 s^{-1}, probably results from surface wave accelerations that disturb the compass readings.

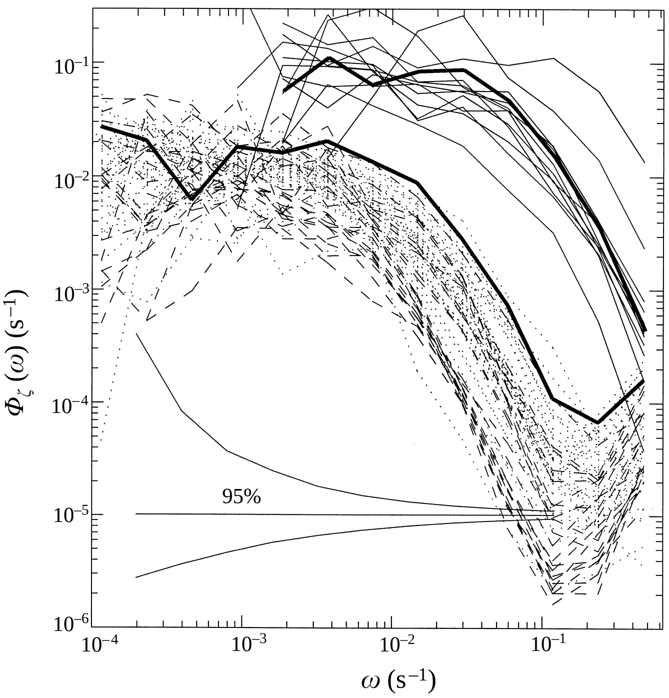

FIGURE 4. As in figure 3, but for averaged vertical vorticity. Two spectra are highlighted (thick solid lines) for clarity.

4. Dimensional analysis for finite sized floats

According to (1.1), oceanic turbulence has fluctuations with scales ranging from the Kolmogorov scale k_η^{-1} (a few millimetres for our data), to the thickness of the turbulent layer, $H \approx 2\pi k_0^{-1}$ (50–100 m in our data). Exact Lagrangian trajectories have fluctuations with these same scales. The float trajectories are smoother than the true Lagrangian trajectory owing to the finite size of the float.

We seek to scale the measured Lagrangian spectra for acceleration and vorticity, Φ_a^F and Φ_ζ^F, as a function of frequency, ω. We assume that the turbulence is parameterized by two parameters, ε and the large-eddy wavenumber k_0, as in (1.1), and that the float is characterized by scales L for acceleration and R for vorticity. These dimensional parameters result in three non-dimensional frequencies: a large-eddy frequency $\omega_0 = \varepsilon^{1/3}k_0^{2/3}$, and float-scale frequencies $\omega_L = \varepsilon^{1/3}L^{-2/3}$ and $\omega_R = \varepsilon^{1/3}R^{-2/3}$. The Kolmogorov frequency, $\omega_\eta = (\varepsilon/\nu)^{1/2}$, does not enter the problem as it is assumed to be much larger than the other frequencies.

At low frequencies, $\omega \ll \omega_L$, we assume that the float size is unimportant and the acceleration spectrum has the general form

$$\Phi_a^F(\omega) = \beta_a \varepsilon B_a(\omega/\omega_0). \tag{4.1}$$

This is the 'large-eddy' scaling.

At higher frequencies, $\omega \gg \omega_0$, we assume that the large-eddy properties are unimportant. The Lagrangian frequency spectrum of the fluid depends only on ε and thus obeys the inertial-subrange scalings from (1.2), $\Phi_a(\omega) = \beta_a\varepsilon$. The Lagrangian frequency spectrum measured by the float has the general form

$$\Phi_a^F(\omega) = \beta_a \varepsilon G_a(\omega/\omega_L), \tag{4.2}$$

where G_a describes the effect of finite float size. We will call this 'float-size' scaling. For $\omega \ll \omega_L$, the float's motion and the fluid's motion are the same, $G_a \to 1$, and the float accurately measures the Lagrangian spectrum of the fluid. We will use the term 'float inertial subrange' for this region to distinguish it from the much larger fluid inertial subrange. The float inertial subrange is marked on several spectra in figure 3.

A similar analysis yields forms for the vorticity spectrum. For $\omega \ll \omega_R$, large-eddy scaling applies, and the general form of the spectrum is

$$\Phi_\zeta^F(\omega) = \beta_\zeta \omega_R B_\zeta(\omega/\omega_0). \tag{4.3}$$

For $\omega \gg \omega_0$, float-size scaling applies, and the general form of the spectrum is

$$\Phi_\zeta^F(\omega) = \beta_\zeta \omega_R G_\zeta(\omega/\omega_R). \tag{4.4}$$

Note that the float does not measure the true fluid vorticity but some average on the scale of R, the drag screen radius. The wavenumber spectrum of vorticity is blue; most of the variance is at the Kolmogorov scale. The smaller the float, the larger the measured r.m.s. vorticity and spectral level. Only if the float is of the Kolmogorov scale or smaller does its rotation rate measure the true fluid vorticity; otherwise the measured vorticity is less than the true vorticity. Thus the float size is an important parameter at all frequencies and appears, through ω_R, in front of the shape functions B_ζ and G_ζ in (4.3) and (4.4).

DFOD found empirical forms for (4.2) and (4.4) based on a subset of the data in figures 3 and 4:

$$\Phi_a^F(\omega) = 1.8\varepsilon \left[1 + 0.17(\omega/\omega_L)^2\right]^{-1}, \tag{4.5}$$

$$\Phi_\zeta^F(\omega) = 1.26\omega_R \left[1 + 2(\omega/\omega_R)^2\right]^{-1}, \tag{4.6}$$

where $L = 0.75$ m (one half of the vertical length of the MLF) and $R = 0.6$ m (the radius of the drag screen) are used in the definitions of ω_L and ω_R, respectively. Equations (4.5) and (4.6) are written in a somewhat different form from those used by DFOD.

5. Model Lagrangian spectra

We now attempt to predict the levels and shapes of the observed vertical acceleration and vorticity spectra. First, we use the approximate wavenumber spectra of homogeneous isotropic turbulence (1.1). The details of the spectrum near the Kolmogorov wavenumber are unimportant since the finite float size attenuates the observed spectrum at a much larger scale. The details of the spectrum near the large-eddy wavenumber are unimportant since the derived Lagrangian frequency spectrum is insensitive to these. Second, we construct a model for the Lagrangian frequency–Eulerian wavenumber spectrum (1.4), following the methods of Fung *et al.* (1992). Third, we assume physical models for the averaging effects of the finite float size. Model Lagrangian frequency spectra for vertical velocity, acceleration and vorticity are then obtained by numerically integrating the frequency–wavenumber spectra over wavenumbers. Empirical analytical approximations to the numerical solutions are found and used in the subsequent data analysis.

5.1. *Wavenumber spectra for isotropic turbulence*

For homogeneous isotropic turbulence, the Eulerian wavenumber spectrum of vertical velocity and vorticity have the forms (Batchelor 1953)

$$\Phi_w(\boldsymbol{k}) = \frac{E(k)}{4\pi k^4}(k_x^2 + k_y^2), \tag{5.1}$$

and

$$\Phi_\zeta(\boldsymbol{k}) = \frac{E(k)}{4\pi k^2}(k_x^2 + k_y^2). \tag{5.2}$$

$E(k)$ is given by (1.1), $\boldsymbol{k}$ is the wave vector, k_x, k_y, and k_z are its components, and k is the wavenumber magnitude. Wavenumber magnitude spectra are defined by integrating the three-dimensional wavenumber spectrum over the spherical shell of constant k:

$$\Phi_w(k) = \tfrac{2}{3}E(k), \tag{5.3}$$

and

$$\Phi_\zeta(k) = k^2\Phi_w(k). \tag{5.4}$$

Note that the velocity spectrum is red ($k^{-5/3}$) in the inertial subrange so most of its variance is at large scales, whereas the vorticity spectrum is blue ($k^{1/3}$) so most of its variance is at small scales. This fundamental difference implies that the finite float size has quite different effects on vorticity and velocity spectra.

5.2. *Float response*

We assume that the float's vertical acceleration, a_F, is the vertical average of the water's vertical acceleration, a, over the float's length. The water's acceleration is assumed to be unaffected by the float. Thus

$$a_F(t) = \int_{-L}^{L} a[x(t), y(t), z(t) + \delta, t]\,\mathrm{d}\delta, \tag{5.5}$$

where the float's path is $[x(t), y(t), z(t), t]$. Spectrally, this is expressed as a wavenumber response function, $H_w(\boldsymbol{k}, L)$, relating the wavenumber spectrum of the water's acceleration, Φ_a, to that of the float, Φ_a^F:

$$\Phi_a^F(\boldsymbol{k}) = \Phi_a(\boldsymbol{k})H_w(\boldsymbol{k}, L), \tag{5.6}$$

$$H_w(\boldsymbol{k}, L) = \mathrm{sinc}^2(k_z L), \tag{5.7}$$

where k_z is the vertical wavenumber, $2L$ is the length of the float, and $\mathrm{sinc}(x) = \sin(x)/x$. Most of the acceleration of the water, and thus of the float, results from pressure gradients which are accurately averaged by the float hull (DFOD). Equation (5.7) is probably an accurate representation of these effects. More complex models of the float response are considered in § 8.

The spin rate of the MLF is more complicated. The MLF rotates owing to the frictional drag of the surrounding flow on the circular screen, particularly its radial fins. The Reynolds number of the fins based on their height (1 cm) and a typical flow past the screen (a few mm s^{-1}) is of order 50, which is transitional between a linear and quadratic drag law. If a linear drag law is used, a linear response model results. This is probably not very accurate, but we use it because there are no easy alternatives. In this case, the measured vertical vorticity is equal to the averaged circulation over the drag screen. The wavenumber response function of the drag screen for vorticity is then

$$H_\zeta(\boldsymbol{k},R)=\left[\frac{8J_2(k_hR)}{k_h^2R^2}\right]^2. \tag{5.8}$$

Here, k_h is the horizontal wavenumber component, R is the radius of the drag screen, and J_2 the Bessel function of the second kind. Equation (5.8) is certainly an oversimplification, ignoring nonlinear drag and the effect of vorticity advection past an imperfectly Lagrangian float. There is no reason to believe that it will produce quantitatively accurate predictions. More complex linear models of the float response are considered in § 8.

5.3. *Transformation from Eulerian to Lagrangian spectra*

For linear waves, the energy distribution in wavenumber and frequency is restricted by dispersion, i.e. $\Phi(\omega,\boldsymbol{k})=\Phi(\boldsymbol{k})\delta[\omega-\Omega(\boldsymbol{k})]$, where $\omega=\Omega(\boldsymbol{k})$ is the dispersion relation. For weakly nonlinear waves, Holloway (1983) suggested that the energy distribution is spread about the linear dispersion curve, i.e. the δ-function broadens, and that the amount of spreading increases with wavenumber.

Unlike waves, turbulence has no dispersion relation. However, there may still be a general relationship between frequency and wavenumber. Fung *et al.* (1992) proposed that 'the energy at each wavenumber is spread over a range of frequencies around a characteristic frequency', ω_k, with a distribution $F(\omega,\omega_k)$. They propose a Gaussian form (their equation (2.13), the 'KSIM' model) which is asymmetric in frequency. We express the same physics as a double Gaussian since we wish to have an expression which is symmetric in frequency,

$$F(\omega,\omega_k)=\frac{1}{(2\pi)^{1/2}\gamma\omega_k}\left\{\exp\left[-\frac{(\omega-\gamma_0\omega_k)^2}{2\gamma^2\omega_k^2}\right]+\exp\left[-\frac{(\omega+\gamma_0\omega_k)^2}{2\gamma^2\omega_k^2}\right]\right\}, \tag{5.9}$$

where $\omega_k=\varepsilon^{1/3}k^{2/3}$. The model has two parameters: γ_0 scales the characteristic frequency associated with wavenumber k, and γ scales the amount of spreading (bandwidth) about this frequency. Since F only redistributes energy, conservation of energy implies $\int_0^\infty F(\omega,\boldsymbol{k})\mathrm{d}\omega=1$. Leslie (1973) suggests that the bandwidth is comparable to the frequency in the inertial subrange, suggesting $\gamma_0=1$ and $\gamma=1$. We follow this choice initially, but then, in § 9.2, investigate the effect of varying the parameters. Nearly the same results are found for a double Gaussian, $\gamma_0=1$, and a single Gaussian, $\gamma_0=0$.

According to this model, the energy at a fixed wavenumber k is distributed within about $2\omega_k$ of the frequency ω_k (figure 5*a*). Since ω_k is proportional to $k^{2/3}$, large (small-k) eddies have long Lagrangian correlation time, i.e. a small frequency bandwidth, and small eddies have a short correlation time. Energy at a fixed frequency ω comes from a wide range of wavenumbers k (or ω_k), with a peak at about 0.6 $\omega^{3/2}\varepsilon^{-1/2}$ and a long tail at higher wavenumbers (figure 5*b*).

5.4. *Model spectra*

We adopt the above concepts to construct the Lagrangian frequency–Eulerian wavenumber spectrum. The spectra of vertical velocity and vorticity are denoted by Φ_ζ and Φ_w, respectively. Spectra of the water's motion have no superscript, i.e. Φ, while those measured by a float have an F superscript, i.e. Φ^F. Expressions for the vertical velocity and vorticity spectra are

$$\Phi_w^F(\omega,\boldsymbol{k})=\Phi_w(\omega,\boldsymbol{k})H_w(\boldsymbol{k},L)=\Phi_w(\boldsymbol{k})F(\omega,\omega_k)H_w(\boldsymbol{k},L), \tag{5.10}$$

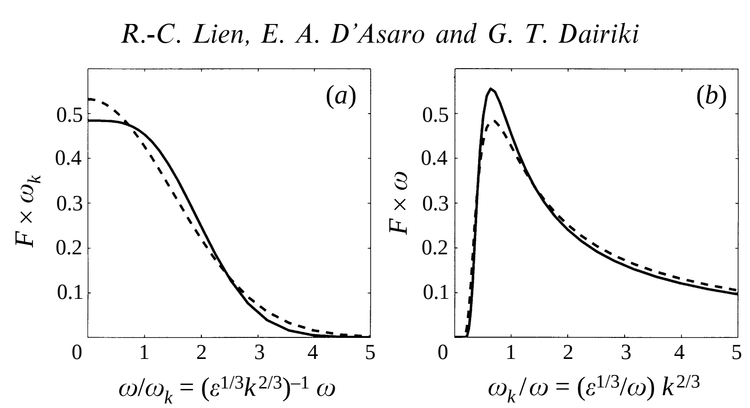

FIGURE 5. The energy distribution function F (5.9) (a) at a fixed wavenumber ω_k and (b) at a fixed frequency ω. Solid lines represent the double Gaussian for $\gamma = \gamma_0 = 1$. Dashed lines show the single Gaussian $\gamma = 1.5$, $\gamma_0 = 0$.

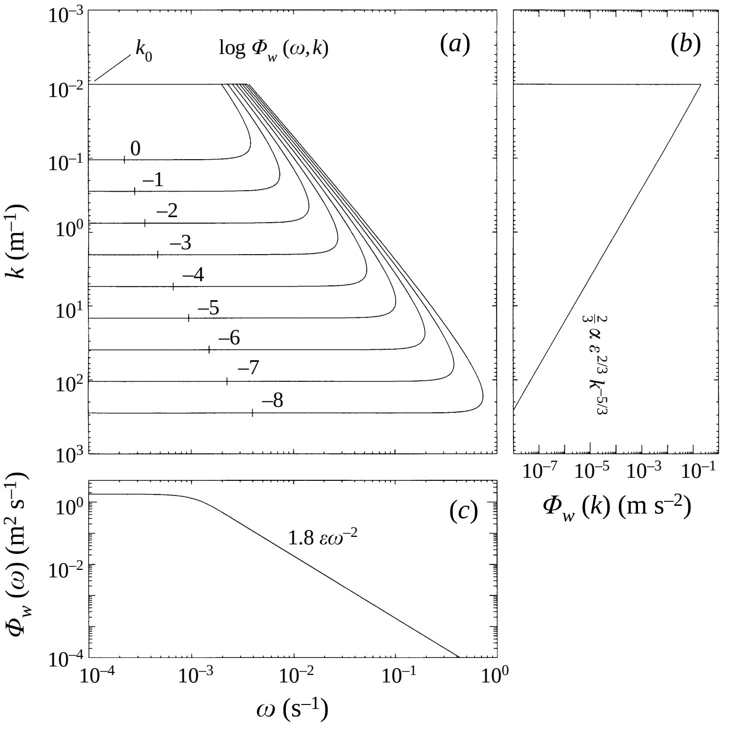

FIGURE 6. (a) Model frequency–wavenumber spectrum of vertical velocity for $\varepsilon = 10^{-6}$ W kg^{-1}. Integrating the joint frequency–wavenumber spectrum over the frequency domain yields the wavenumber spectrum (b) and integrating over the wavenumber domain yields the frequency spectrum (c).

and

$$\Phi^F_\zeta(\omega,\boldsymbol{k}) = \Phi_\zeta(\omega,\boldsymbol{k})H_\zeta(\boldsymbol{k},R) = \Phi_\zeta(\boldsymbol{k})F(\omega,\omega_k)H_\zeta(\boldsymbol{k},R). \tag{5.11}$$

Each wavenumber–frequency spectrum is the product of a wavenumber spectrum, the spreading function, F, and, for the float spectra, an instrument response function, H.

A contour plot of the frequency–wavenumber spectrum (5.10) of vertical velocity, Φ_w, is shown in figure 6(a) for $\varepsilon = 10^{-6}$ W kg^{-1} and $k_0 = 0.01\,$m^{-1}. The frequency

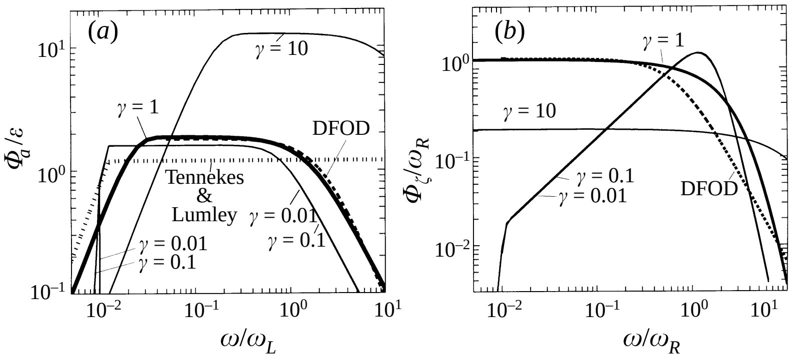

FIGURE 7. Normalized model Lagrangian frequency spectra of (*a*) vertical acceleration and (*b*) vertical vorticity for different γ (solid lines) compared with the DFOD empirical spectrum (thick dashed line) and the spectrum proposed by Tennekes & Lumley (1972).

bandwidth increases with wavenumber. Projection onto the wavenumber domain reduces to the $k^{-5/3}$ spectrum (figure 6*b*), and projection onto the frequency domain yields a Lagrangian frequency spectrum that is white below the large-eddy frequency and has an ω^{-2} form in the inertial subrange (figure 6*c*).

Multiplying the vertical velocity frequency spectrum by ω^2 yields the vertical acceleration spectrum. The forms of the vertical acceleration and vorticity spectra, including float response functions, are expressed in spherical coordinates ($k_x = k\cos(\phi)\sin(\lambda), k_y = k\sin(\phi)\sin(\lambda), \text{and}\, k_z = k\cos(\lambda)$) as

$$\Phi_a^F(\omega) = \alpha\varepsilon\omega^2 \int_{\omega_0}^{\infty} \mathrm{d}\omega_k \omega_k^{-2} F(\omega, \omega_k) \left\{ \int_0^{\pi} \mathrm{d}\lambda \tfrac{3}{4} \sin^3 \lambda H_w(\omega_k, \omega_L, \lambda) \right\}, \tag{5.12}$$

and

$$\Phi_\zeta^F(\omega) = \alpha \int_{\omega_0}^{\infty} \mathrm{d}\omega_k \omega_k F(\omega, \omega_k) \left\{ \int_0^{\pi} \mathrm{d}\lambda \tfrac{3}{4} \sin^3 \lambda H_\zeta(\omega_k, \omega_R, \lambda) \right\}, \tag{5.13}$$

where $\omega_0 = \varepsilon^{1/3} k_0^{2/3}$ is the large-eddy frequency corresponding to the large-eddy wavenumber k_0 in (1.1). The terms in the curly brackets represent instrumental effects and are equal to 1 for point measurements.

Model Lagrangian frequency spectra of vertical acceleration non-dimensionalized by 'float-size' scaling are shown in figure 7(*a*) for different values of γ. Constant values of $\gamma_0 = 1$ and $\omega_0/\omega_L = 0.01$ are used. These are compared with the model spectrum proposed by Tennekes & Lumley (1972) and the DFOD empirical spectrum. All model spectra have a similar shape, but the level and roll-off frequency agree only with the DFOD spectrum for γ near 1.

The shape of the model spectrum of vorticity is, in contrast to that of acceleration, extremely sensitive to the bandwidth, γ (figure 7*b*). Model spectra for $\gamma < 1$ are blue in the inertial subrange, as predicted by dimensional analysis which does not include R. For $\gamma \geqslant 1$, model spectra are flat in the inertial subrange in agreement with the observations. For $\gamma = 1$, the spectral level nearly matches the DFOD data fit, but the shape of the high-frequency roll-off is wrong. For $\gamma > 1$, the spectral level is lower than observed.

Overall, the model spectra agree best with the DFOD spectra for $\gamma_0 = 1$ and $\gamma = 1$. These values also yield a model acceleration spectrum that is blue below the inertial subrange, as suggested by Tennekes & Lumley (1972) (1.2). We therefore use

$\gamma_0 = \gamma = 1$ for comparison with the data. The numerically computed model spectra are accurately described by the following empirical analytical forms:

$$\Phi_a^F(\omega) = 1.8\varepsilon \left[1 + \left(2.2\frac{\omega_0}{\omega}\right)^4\right]^{-0.5} \left[1 + \left(0.63\frac{\omega}{\omega_L}\right)^2\right]^{-0.8}, \tag{5.14}$$

$$\Phi_\zeta^F(\omega) = 1.2\omega_R \left[1 + \left(0.22\frac{\omega}{\omega_R}\right)^{1.5}\right]^{-4}. \tag{5.15}$$

6. Observed and model spectra

6.1. *Model fitting*

We now do a more formal comparison of observed and modelled spectral shapes. The model spectrum (5.14) is fitted to each observed acceleration spectrum, to estimate ε and ω_0 for that spectrum. The observed acceleration and vorticity spectra are scaled by these parameters in order to determine whether the observed spectra have common shapes and whether those shapes are consistent with the model.

Ideally, an estimate of ε should be made only in the float inertial subrange $\omega_0 \ll \omega \ll \omega_L$. However, in these data, ω_L is at most a factor of 10 above ω_0 and often less. There are not enough data in this limited spectral range to make statistically reliable estimates of ε for each spectrum. Statistically reliable fits can be made only by including frequencies near ω_L. Our values of ε thus necessarily depend on the assumed form of the float response function. Although we use the analytical forms of the response function implicit in (5.14) and (5.15), these are consistent with the data. The role of theory is therefore primarily to determine the dimensional form of the float response, i.e. (4.2), and only secondarily to show that the observed shape is consistent with a simple physical model.

For the model acceleration spectrum,

$$\omega_0 = \varepsilon\sigma_w^{-2}h_{\sigma_w}, \tag{6.1}$$

where σ_w^2 is the variance of vertical velocity, and h_{σ_w} is the ratio between the vertical velocity variance of the water and that of the float computed from the model spectrum; ω_0 is estimated using (6.1) for each spectrum. The model spectrum (5.14) is fitted to the observed acceleration spectra shown in figure 3 by minimizing the mean-square deviation between the model and the data as a function of ε. If ω_{noise} is the frequency where the observed spectrum equals the instrumental digitization noise spectrum, the minimization is done to include all spectral estimates up to 0.5 ω_{noise}. Since the wavelet spectral estimators are logarithmically spaced, $\omega\Phi_a$, rather than Φ_a, is fitted so as to weight each estimate by its degrees of freedom.

6.2. *Acceleration*

The observed acceleration spectra, non-dimensionalized using the 'float-size' scaling, are shown in figure 8(*b*). Only spectral estimates with $\omega > 0.6\,\omega_0$ are plotted. The same spectra, non-dimensionalized using the 'large-eddy' scaling, are shown in figure 8(*a*). Only spectral estimates with $\omega < 0.2\,\omega_L$ are plotted. Also shown are composite spectra (heavy lines), obtained by averaging the non-dimensional spectra. Shading indicates 95% confidence limits computed assuming Gaussian statistics; the error bars indicate 95% confidence limits computed using the bootstrap method (Efron & Gong

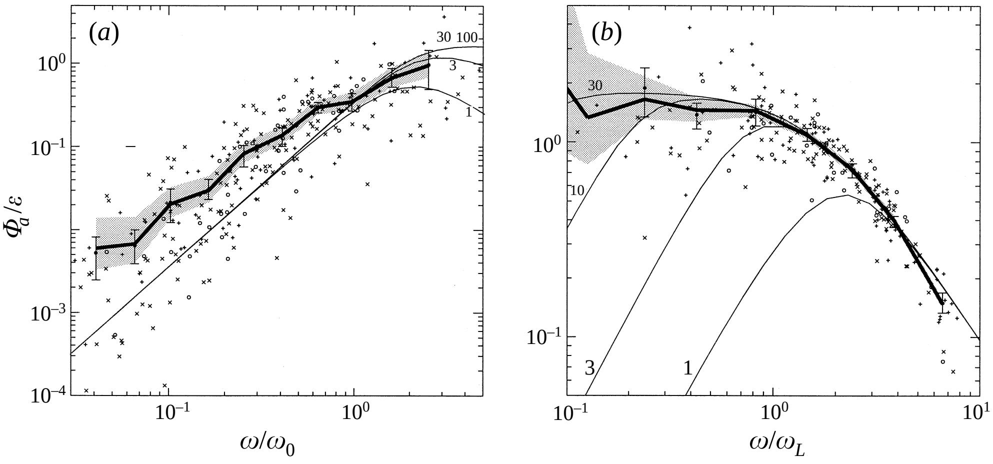

FIGURE 8. Non-dimensionalized Lagrangian acceleration spectra. The spectra from figure 3 have been non-dimensionalized using (*a*) the 'large-eddy' and (*b*) 'float-size' scaling. Data from tidal channels are denoted by ○, from convective-mixed layers by +, and from wind-driven mixed layers by ×. The average of these data, the 'composite spectrum', is shown by the heavy curve. Confidence levels (95%) are computed assuming Gaussian statistics (shading) and the bootstrap method (error bars). Thin solid lines show the model spectra (5.14) for $\omega_L/\omega_0=1$, 3, 10, and 30.

1983). The two error estimates are similar, indicating that the wavelet coefficients have an approximately Gaussian distribution. Scaling greatly reduces the variations of the spectral levels (compare figures 3 and 8).

The composite spectra show a short float inertial subrange bounded at high ($\approx \omega_L$) and low ($\approx \omega_0$) frequencies by regions with spectral slopes of about -2 and $+2$ respectively. In the float-size scaling the model and composite spectra agree very well, except that the composite spectrum lies about 15% below the model spectrum in the inertial subrange. This difference is marginally significant at best. In the large-eddy scaling, significant universality is apparent even for frequencies well below ω_0. Here, the composite spectrum has a flatter slope than the model, rising significantly above it at the lowest frequencies.

6.3. *Vorticity*

Figure 9 shows the vorticity spectra after non-dimensionalization using the float-size and large-eddy scalings. There are no free parameters; the value of ε used in the normalization is that estimated from the corresponding acceleration spectrum. Nevertheless, the vorticity spectra collapse to a universal curve nearly as well as the acceleration spectra do. This is clear evidence that ε and ω_0 are the appropriate scaling parameters.

The composite vorticity spectrum was estimated by averaging the non-dimensional vorticity spectra. In figure 9(*a*), the large-eddy scaling, the composite and model spectra are white, but the composite has a slightly higher level. In figure 9(*b*), float-size scaling, the model and composite spectra agree in the inertial subrange, but have different shapes in the instrumental roll-off region. Thus, although the vorticity spectra scale as described by (4.4) and have a universal shape, G_ζ, this shape is not well predicted by (5.8). This is not surprising since the linear drag law used to derive (5.8) is not very accurate.

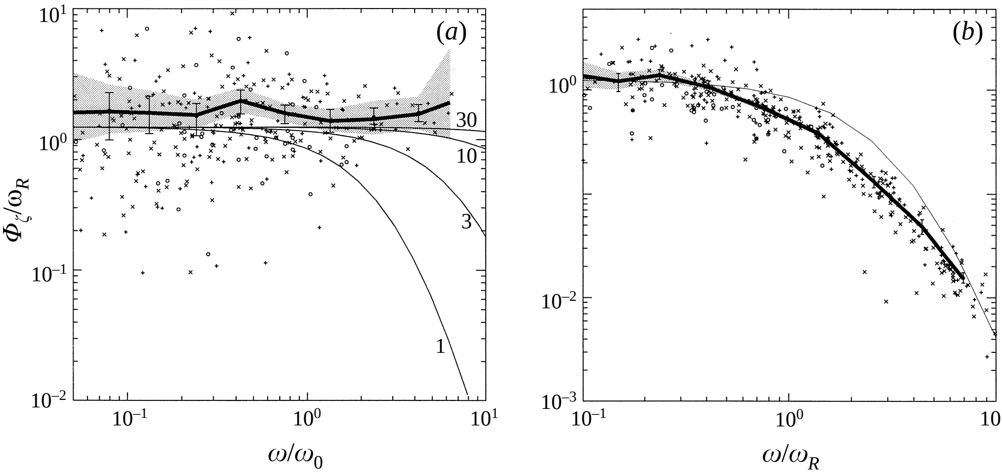

FIGURE 9. As in figure 8, but for vorticity spectra. (*a*) Large-eddy scaling. Thin lines show model spectrum (5.15) for ω_R/ω_0= 1, 3, 10, and 30. (*b*) Float-size scaling. A single thin line shows the model spectra for all values of ω_R/ω_0.

7. The Kolmogorov constants

The forgoing analysis contains no independent estimate of the Kolmogorov constants β_a and β_ζ since no independent estimates of ε were made. Using data from a convective boundary layer (figure 2), ε can be estimated from the buoyancy flux and Φ_a can be estimated from the floats. This will yield estimates of the Kolmogorov constants.

A steady-state convectively driven ocean mixed layer with no surface wind, wave breaking, mean shear or entrainment is governed by only two parameters: the (cooling) surface buoyancy flux, J_b, and the layer depth, H. The buoyancy flux decays linearly from J_b at the surface to 0 at H. The turbulence kinetic energy equation for the boundary layer then reduces to a balance of production by buoyancy and dissipation, or

$$\overline{J}_b = \overline{\varepsilon}, \tag{7.1}$$

where $\overline{J}_b$ is the averaged buoyancy flux and $\overline{\varepsilon}$ is the average viscous dissipation rate (Anis & Moum 1994). We will estimate $\overline{J}_b$, and thus $\overline{\varepsilon}$, by three independent methods for a subset of the data in figure 2.

First, we estimate the buoyancy flux from the average rate of change of temperature, $\mathrm{d}\overline{\theta}/\mathrm{d}t$. If all the temperature change is due to the surface flux,

$$\overline{J}_{b\theta} = \frac{\alpha_\theta g H}{2}\frac{\mathrm{d}\overline{\theta}}{\mathrm{d}t}, \tag{7.2}$$

where α_θ is the thermal expansion rate of sea water. For a given trajectory, temperature data are binned by depth, and the least-squares estimate of $\mathrm{d}\overline{\theta}/\mathrm{d}t$ is found for each depth. These $\mathrm{d}\overline{\theta}/\mathrm{d}t$ values are averaged, excluding outlier values at the top and bottom of the mixed layer. H is taken as the maximum depth of the float during the trajectory.

Second, we estimate the average buoyancy flux from the average covariance of vertical velocity and temperature (Tennekes & Lumley 1972):

$$\overline{J}_{bC1} = \frac{g\alpha_\theta}{T}\int_0^T w'\theta'\mathrm{d}t\left(\frac{H}{2(\overline{H+z})}\right), \tag{7.3}$$

where the integral is taken along a float trajectory. Integration by parts yields an equivalent expression in the limit as $T \to \infty$:

$$\overline{J}_{bC2} = -\frac{g\alpha_\theta}{T}\int_0^T z'\frac{\mathrm{d}\theta'}{\mathrm{d}t}\mathrm{d}t\left(\frac{H}{2(\overline{H+z})}\right). \tag{7.4}$$

The values of $\overline{J}_{bC1}$ and $\overline{J}_{bC2}$ are different for finite T and more reliable values are found by averaging them:

$$\overline{J}_{bC} = (\overline{J}_{bC1} + \overline{J}_{bC2})/2. \tag{7.5}$$

If the float spends equal time at all depths in a mixed layer of depth H, then the average of $w'\theta'$ equals the temperature flux averaged over depth. In fact, the floats were made slightly lighter than the water in order to keep them in the mixed layer. They therefore spent somewhat more time in the upper part of the mixed layer. Since the heat flux is larger in this region, the unequal depth distribution of the floats biases the estimated heat flux. A correction was made by assuming a heat flux profile decaying to zero at depth H. In this case the heat flux, averaged over depth, should be corrected by the factor $\frac{1}{2}H/(\overline{H+z})$ as in (7.3) and (7.4). Computationally, the time series of z, w, θ, and $\mathrm{d}\theta/\mathrm{d}t$ are de-meaned and detrended in time and depth to form the perturbation quantities. These data are passed through a maximal overlap wavelet transform using Daubechies fourth-order wavelets (Press *et al.* 1988), and the covariances are computed from the wavelet products. Wavelets with periods longer than 5.5 hours are not included in the covariances, since they are poorly resolved and well below the peak in the covariance spectrum.

Finally, we estimate the surface heat flux, Q_0, from meteorological measurements described by DFOD and find the average buoyancy flux,

$$\overline{J}_{bQ} = \frac{g\alpha_\theta}{2\rho C_p}Q_0, \tag{7.6}$$

where ρC_p is the specific heat of sea water and the factor of 2 converts surface flux to depth-average flux. The fluxes are dominated by long-wave radiation and latent heat. The best estimates of Q_0 have bias errors of 10 Wm^{-2} (Hosom *et al.* 1995). We undoubtedly do worse. It seems unlikely that the error in our estimates is less than 15%.

Estimates were made using MLF and meteorological measurements from 2200 to 0600 local time during five nights (nine float deployments) chosen to have very weak surface winds (see figure 2) and nearly clear skies. The choice of this time period is a compromise between having more than two mixed layer overturnings and allowing the mixed layer to reach its equilibrium depth so that a steady state can be assumed.

Averaged over all float trajectories, $\overline{J}_{b\theta} = 3.5 \times 10^{-8}$ W kg^{-1}, $\overline{J}_{bC} = 3.2 \times 10^{-8}$ W kg^{-1} and $\overline{J}_{bQ} = 2.7 \times 10^{-8}$ W kg^{-1}. $\overline{J}_{bQ}$ and $\overline{J}_{bC}$ differ by about 25%, while the two float-based estimates, $\overline{J}_{bC}$ and $\overline{J}_{b\theta}$, differ by 9%. The float-based estimates have fewer sources of error than the meteorological estimates, but we cannot otherwise show that they are more accurate. We will use $\overline{J}_b = (\overline{J}_{bC} + \overline{J}_{b\theta})/2$ to scale the spectra. On all but one night, two floats were deployed; the average of the two buoyancy flux estimates is used to scale both spectra. These estimates neglect buoyancy due to salinization of the sea surface by evaporation. Based on the estimates

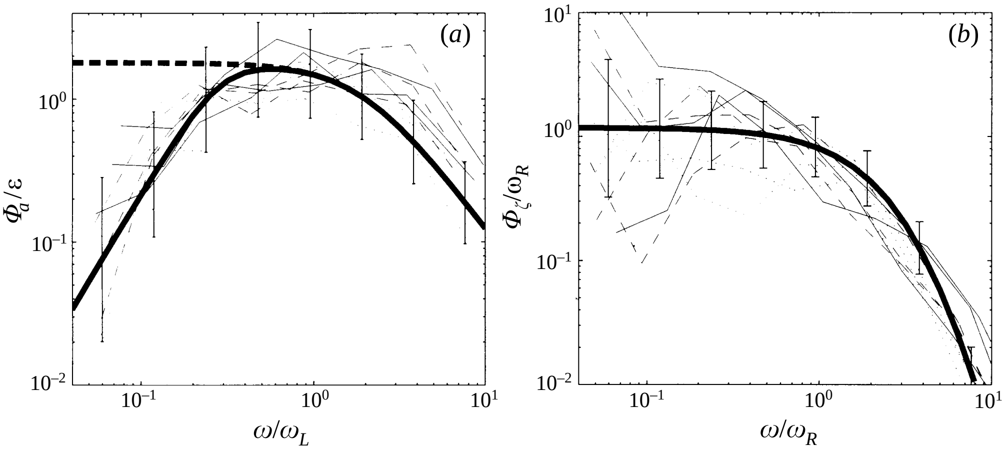

FIGURE 10. Non-dimensional spectra of (*a*) acceleration and (*b*) vorticity for convective boundary layer data. Heavy line shows model spectra. Light lines (dashed, dotted and solid) show the individual spectra. Bars show the 95% confidence levels for individual spectra and include uncertainties in both the spectral level and the value of ε. The uncertainty in the average spectrum is about 1/3 of this. The dashed line in (*a*) shows the model spectrum assuming $\omega_0 = 0$. The intercept of this line with the left-hand axis gives the value of the Kolmogorov constant β_a; the corresponding intercept in (*b*) gives β_ζ.

of latent heat flux, evaporation will increase the J_b by about 7% which is a small correction compared to other errors. The statistical error in J_b for any given evening, estimated from the average difference between $\overline{J}_{bC}$ and $\overline{J}_{b\theta}$, is about 30%.

Figure 10(*a*) shows the non-dimensionalized acceleration spectra (light lines). Only the float-size non-dimensionalization is shown, because ω_L/ω_0 is nearly the same for all spectra. The model spectrum computed using an average ω_0 is shown by the dark line; the model spectrum computed with $\omega_0 = 0$ is shown by the dashed line. The nine scaled acceleration spectra fall mostly within the 95% confidence limits of the model, although some show systematic deviations at high frequency. The value of β_a is given by the level of the inertial subrange; it lies between 1 and 2.

Figure 10(*b*) similarly shows the non-dimensionalized vorticity spectra (light) and model spectrum (heavy). The data fall below the model in the instrumental fall-off region, as is also seen in figure 9. At low frequencies the data are more variable than the expected error. The value of β_ζ is between about 0.6 and 1.8.

8. Float models

Two simplified models of the float behaviour are used in the foregoing analysis: the float's acceleration is the average of the water's acceleration over the float's length, and the float's spin rate is the average of the circulation over the drag screen. In reality, the float consists of both elements, and undoubtedly influences the flow around it. In figure 11 we explore the effects of different assumptions. Spectra are shown which assume an infinitesimal float ('Perfect sensor'), an average over the vertical length of the float ('Vertical average'), an average over the drag screen ('Disk average') and a perfect spectral averaging ('Top-hat cutoff') in which the float responds perfectly to motions below a fixed wavenumber and not at all to motions above that wavenumber. The cutoff wavenumber was chosen so that the spectral level at low frequency agrees with that of the other models. The composite acceleration spectrum from figure 8 is

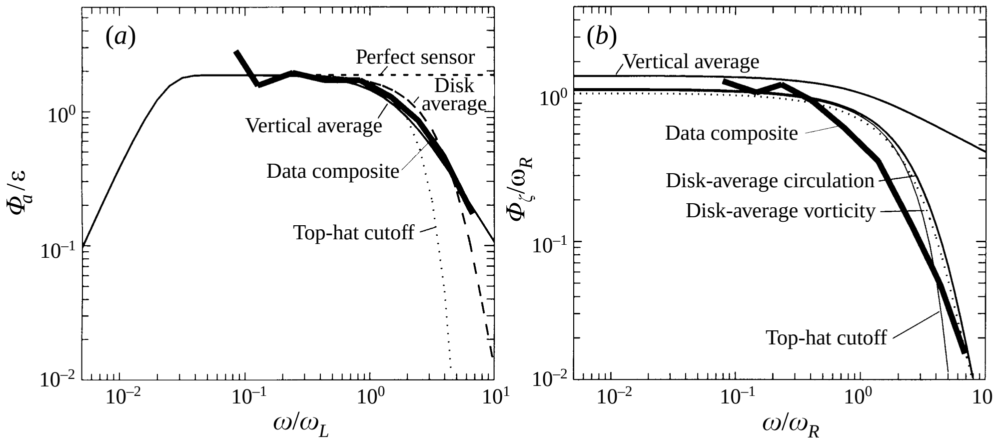

FIGURE 11. Normalized model spectra of (*a*) vertical acceleration and (*b*) vertical vorticity for various models of the float response. Composite spectra from figures 8 and 9 are shown for reference (thick solid lines).

shown for reference ('Data composite'). Its level has been adjusted slightly to match the model spectral level at low frequency. This is equivalent to changing the model parameters slightly.

The acceleration spectra (figure 11*a*) are insensitive to the float model for frequencies up to $2\omega_L$. The 'Vertical average' and 'Disk average' spectra are very similar, so that, given other uncertainties, it is impossible to say what linear combination of them best fits the data. The highly unphysical 'Top-hat' model differs little from these near ω_L. Apparently, the spectral spreading function, $F(\omega, \omega_k)$, smooths all of these spectra into approximately the same shape near ω_L so their differences become apparent only at higher frequencies. Because most of the variance in the acceleration spectrum is near ω_L, the estimation of ε from the acceleration spectra (§ 6.1) is relatively insensitive to the details of the float response model.

In contrast, the vorticity spectrum (figure 11*b*) is quite sensitive to the float response model. Because vorticity has a blue wavenumber spectrum, the vorticity variance, and thus the spectral level, depends on the high-wavenumber cutoff, which is set by the averaging scale of the float. In (4.4), the spectral level is proportional to ω_R and thus $R^{2/3}$. Thus, in figure 11(*b*) the 'Vertical average' model leads to a very different model spectrum at all frequencies than models which average vorticity ('disk-average vorticity') or circulation ('disk-average circulation') over the drag disk. These produce a spectrum with the proper spectral level, but a roll-off frequency slightly greater than observed. The 'top-hat' cutoff model produces a spectrum similar to that of disk-averaged vorticity and disk-averaged circulation but with a steeper slope at high frequency. None of these simple models reproduces both the spectral level observed at low frequencies and the instrumental roll-off observed at high frequencies. The rotation rate of the float can apparently be modelled as a spatial average of vorticity only for low frequencies. At frequencies greater than ω_R the physics must be more complex. This is also clear from the hydrodynamics; the frictional coupling between the drag screen and the water is probably nonlinear and may well depend on the imperfect water-following ability of the float. Thus, although the measured spectra of float rotation rate at frequencies above ω_L clearly scale with ε, their relationship to the fluid vorticity is unclear.

9. Discussion and summary

9.1. *Inertial subranges*

Ideally, the existence of the Lagrangian frequency inertial subrange should be established by measuring the appropriate spectral slope over several decades in frequency as described in the classic paper by Grant *et al.* (1962). The Kolmogorov constant is then easily found from the spectral level in this frequency range. Our analysis indicates that the part of the inertial subrange unaffected by float size is bounded by approximately $2\omega_0$ and $\omega_L/2$. These have a ratio of approximately $(H/4L)^{2/3}$, or about 3 for a 1 m float in a 50 m thick turbulent layer. To obtain a wider float inertial subrange, either a smaller float, or a thicker turbulent layer would be required.

Here, an indirect approach has been used. Figures 8 and 9 establish that the observed spectra scale only with ε at high frequencies (above ω_L) and that the same values of ε scale both acceleration and vorticity spectra. The non-dimensional spectral shapes depend on the properties of the float. The dimensional arguments of § 4 and plausible models for the wavenumber–frequency spectrum of turbulence (figure 6) and float behaviour (5.5), results in a prediction of the spectral shapes (5.14). The resulting model spectra agree with the measured acceleration spectra at all frequencies (figure 8). Furthermore, the model spectra are insensitive to the details of the float model (figure 11*a*). The effect of the float response to acceleration can therefore be removed from measured acceleration spectra and an inertial subrange approximately one decade wide can be measured. This is used to estimate the Kolmogorov constant for acceleration in § 7.

The corresponding calculation for vorticity is less satisfactory, both because the model vorticity spectrum does not agree with the observed spectrum except at low frequency (figure 9) and because its shape is sensitive to the model details (figure 11*b*). This is consistent with the weak physical basis for the linear relationship between float spin rate and vorticity assumed in the model.

The Kolmogorov constant, $\beta_a = \Phi_a/\varepsilon$, is estimated to be between 1 and 2. This is consistent with previous estimates if the likely factors of 2 and 2π are included. Uncertainty in β_a limits the accuracy of ε estimates made from acceleration spectra. This limited accuracy is primarily due to statistical uncertainties, resulting from the limited amount of data. We hope to remedy this soon.

9.2. *The Eulerian–Lagrangian transformation*

The Lagrangian frequency–Eulerian wavenumber spectrum (figure 6) is constructed by spreading the energy at each Eulerian wavenumber over a range of frequencies given by a spreading function, $F(\omega, \omega_k)$ (5.9). For $\gamma = \gamma_0 = 1$, F is the sum of two Gaussians (figure 5*a*, solid line). For $\gamma_0 = 0$ a true Gaussian shape is found (figure 5*a*, dashed line). For various values of γ and γ_0 different spectral shapes and different values of β_a are predicted.

The data constrain γ and γ_0. Reasonable agreements in spectral shape and Kolmogorov constant are obtained only for $\gamma_0 < 1.3$ and $0.9 < \gamma < 1.7$. Note that γ_0 may be zero, i.e. we cannot determine if F is better described by a single or double Gaussian. Other forms for F are also satisfactory: algebraic functions similar in shape to a Gaussian or the sum of two squared or square-rooted Gaussians produce spectral shapes for the vorticity and acceleration spectra very similar to those shown here. The data appear to constrain only the approximate width of the energy spreading function and support the proposed dependence on ε and κ.

9.3. *Lagrangian spectral shapes*

The model used here provides a simple explanation for the shapes of Lagrangian frequency spectra. Energy at Eulerian wavenumber k is spread uniformly over Lagrangian frequencies less than ω_k, but little energy is spread to frequencies larger than $2\omega_k$ (figure 5*a*). Since most of its variance in vorticity is at high wavenumbers, the Lagrangian frequency spectrum of vorticity is white. The spectral level is determined by the highest wavenumber in the spectrum, either the Kolmogorov or float scale. Similarly, the spectrum of vertical velocity wavenumber has peak at the large-eddy wavenumber k_0, so the Lagrangian frequency spectrum of vertical velocity is white below the large-eddy frequency ω_0. Above the large-eddy wavenumber, the vertical velocity spectrum is red, so the spreading to higher frequencies is weak and can be ignored. Accordingly, the Lagrangian frequency spectrum can be derived by equating the energy near Eulerian wavenumber k to that near Lagrangian frequency ω_k. The acceleration spectrum in the inertial subrange is thus insensitive to the shape of the spreading function (figure 7) as well as to the float response function.

9.4. *Universality of the spectral shapes*

The data presented here clearly show that spectra of Lagrangian acceleration and vorticity in oceanic boundary layers tend to have universal forms when properly scaled, even at low frequencies. The spectra appear to be accurately parameterized by models with only two parameters, ω_0 and ε. This may serve as a partial justification for using two-equation turbulence models based on near-equilibrium dynamics to predict the behaviour of oceanic boundary layers.

A great many people have played important roles in making these measurements. We particularly thank Dr David Farmer for a long and productive collaboration. We thank Drs Fung and Hanna for their help in interpreting their earlier studies. A critical reviewer was very helpful in clarifying our thoughts. This work was supported by Office of Naval Research grant N00014-94-J-0024 and National Science Foundation grant OCE9301835.

REFERENCES

Anis, A. & Moum, J. N. 1994 Prescriptions for heat flux and entrainment rates in the upper ocean during convection. *J. Phys. Oceanogr.* **24**, 2142–2155.

Batchelor, G. K. 1953 *The Theory of Homogeneous Turbulence*. Cambridge University Press.

Corrsin, S. 1963 Estimates of the relations between Eulerian and Lagrangian scales in large Reynolds number turbulence. *J. Atmos. Sci.* **20**, 115–119.

D'Asaro, E. A. & Dairiki, G. T. 1997 Turbulence measurements in a wind driven mixed layer. *J. Phys. Oceanogr.* **27**, 2009–2022.

D'Asaro, E. A., Farmer, D. M., Osse, J. T. & Dairiki, G. T. 1996 A Lagrangian float. *J. Atmos. Ocean. Technol.* **13**, 1230–1246 (referred to herein as DFOD).

Efron, B. & Gong, G. 1983 A leisurely look at the bootstrap, jackknife and cross-validation. *Am. Statist.* **37**, 36–48.

Fung, J. C. H., Hunt, J. C. R., Malik, N. A. & Perkins, R. J. 1992 Kinematic simulation of homogeneous turbulence by unsteady random Fourier modes. *J. Fluid Mech.* **236**, 281–318.

Grant, H. L., Stewart, R. W. & Moilliet, A. 1962 Turbulence spectra from a tidal channel. *J. Fluid Mech.* **12**, 241–268.

Hanna, S. R. 1980 Phoenix Lagrangian turbulence observations using Pibals and Tetroons. In *Project Phoenix: the September 1978 Field Operations* (ed. W. H. Hooke). NOAA/NCAR Report, Boulder Atmospheric Observatory, No. 1.

Hanna, S. R. 1981 Lagrangian and Eulerian time-scale relation in the daytime boundary layer. *J. Appl. Met.* **20**, 242–249.

Holloway, G. 1983 A conjecture relating oceanic internal waves and small-scale processes. *Atmos.–Ocean.* **21**, 107–122.

Hosom, D. S., Weller, R. A., Payne, R. E. & Prada, K. E. 1995 The IMET (improved meteorology) ship and buoy system. *J. Atmos. Ocean. Technol.* **12**, 527–540.

Kaneda, Y. 1993 Lagrangian and Eulerian time correlations in turbulence. *Phys. Fluids* A **5**, 2835–2845.

Kolmogorov, A. N. 1941 The local structure of turbulence in incompressible viscous fluid for very large Reynolds numbers. *Dokl. Akad. Nauk SSSR* **30**, 299–303.

Leslie, D. C. 1973 *Developments in the Theory of Turbulence*. Clarendon.

Melville, W. 1996 The role of surface wave breaking in air-sea interaction. *Ann. Rev. Fluid Mech.* **28**, 279–321.

Percival, D. B. & Guttorp, P. 1994 Long-memory processes, the Allan variance and wavelets. In *Wavelets in Geophysics* (ed. E. Foufoula-Georgiou & P. Kumar), pp. 325–343. Academic.

Press, W. H., Flannery, B. P., Teukolsky, S. A. & Vetterling, W. T. 1988 *Numerical Recipes in C: the Art of Scientific Computing*, 2nd edn. Cambridge University Press.

Sreenivasan, K. 1995 On the universality of the Kolmogorov constant. *Phys. Fluids* **7**, 2778–2784.

Tennekes, H. & Lumley, J. L. 1972 *A First Course in Turbulence*. MIT Press.